The inverse perovskite BaLiF$_3$: single-crystal neutron diffraction and analyses of potential ion pathways

Dennis Wiedemann, Falk Meutzner, Oscar Fabelo and Steffen Ganschow

The inverse perovskite BaLiF₃: single-crystal neutron diffraction and analyses of potential ion pathways

Dennis Wiedemann,[a]* Falk Meutzner,[b,c] Oscar Fabelo[d] and Steffen Ganschow[e]

[a]Institut für Chemie, Technische Universität Berlin, Strasse des 17. Juni 135, Berlin, 10623, Germany, [b]Institut für Experimentelle Physik, TU Bergakademie Freiberg, Leipziger Strasse 23, Freiberg, 09596, Germany, [c]Samara National Research University, Moskovskoye Shosse 34, Samara, 443086, Russian Federation, [d]Institut Laue Langevin, 71 Avenue des Martyrs, CS 20156, Grenoble Cedex 9, 38042, France, and [e]Leibniz-Institut für Kristallzüchtung, Max-Born-Strasse 2, Berlin, 12489, Germany. *Correspondence e-mail: dennis.wiedemann@chem.tu-berlin.de

Doped barium lithium trifluoride has attracted attention as component for scintillators, luminescent materials and electrodes. With lithium and fluoride, it contains two possibly mobile species, which may account for its ionic conductivity. In this study, neutron diffraction on oxide-containing BaLiF₃ single-crystals is performed at up to 636.2°C. Unfortunately, ion-migration pathways could not be mapped by modelling anharmonic ion displacement or by inspecting the scattering-length density that was reconstructed via maximum-entropy methods. However, analyses of the topology and bond-valence site energies derived from the high-temperature structure reveal that the anions can migrate roughly along the edges of the LiF₆ coordination octahedra with an estimated migration barrier of ∼0.64 eV (if a vacancy permits), whereas the lithium ions are confined to their crystallographic positions. This finding is not only valid for the title compound but for ion migration in all perovskites with Goldschmidt tolerance factors near unity.

1. Introduction

Since the early 2000s, fluoride perovskites have attracted attention because of their prospective application in semiconductors, optoelectronics and chemosensorics. More specifically, the inverse cubic perovskite BaLiF₃ is contemporarily discussed, e.g. as a component for scintillators (Kurosawa et al., 2017), luminescent materials (Qiang et al., 2016) or specialized arc-welding electrodes (Wang, 2014).

BaLiF₃ is of the perovskite CaTiO₃-type and crystallizes in the space group $Pm\bar{3}m$ with $a \simeq 3.992$ Å (Ludekens & Welch, 1952). The fluoride ions form octahedra around the lithium and cuboctahedra around the barium ions, whereas they themselves are coordinated in the fashion of a compressed square bipyramid. The term 'inverse perovskite'[1] signifies that, in contrast to the situation in a normal perovskite, the cation of the higher charge occupies the position with the higher coordination number (Roy, 1954). The Goldschmidt tolerance factor (Goldschmidt, 1926), calculated herein with ionic radii according to Shannon (1976), illustrates why this is the case: $t = 0.995$ for the inverse configuration shows an almost ideal radii relation, whereas $t = 0.594$ (calculated using the radius of a lithium ion in eightfold coordination) is clearly out of range

© 2018 International Union of Crystallography

---

[1] Inverse perovskites should not be confused with antiperovskites, in which the role of cations and anions are interchanged with respect to normal perovskites.
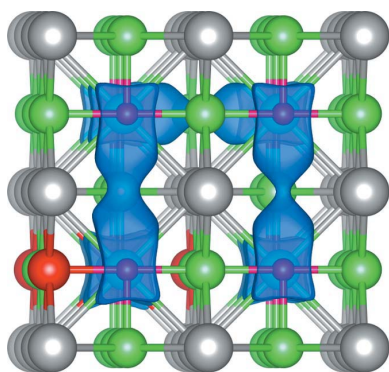
Table 1
Experimental details.

For all structures: $BaLiF_{2.8}O_{0.1}$, $M_r = 199.1$, cubic, $Pm\bar{3}m$, $Z = 1$, $\mu = 0.05$ mm, crystal size (mm): $5.00 \times 5.00 \times 5.00$. Experiments were carried out with neutron radiation, $\lambda = 0.83860$ Å using the hot-neutron four-circle diffractometer D9. Extinction was corrected for using a *SHELXL*-type expression (Sheldrick, 2015), $F_c^* = kF_c[1 + 0.001xF_c^2\lambda^3/\sin(2\theta)]^{-\frac{1}{4}}$.

	26.8°C	412°C	555°C	636.2°C
Crystal data				
a (Å)	3.9978 (2)	4.0406 (2)	4.0581 (3)	4.0763 (4)
V (Å^3)	63.90 (1)	65.97 (1)	66.83 (2)	67.73 (2)
Data collection				
T_{min}, T_{max}	0.975, 0.978	0.975, 0.978	0.976, 0.979	0.976, 0.979
No. of measured, independent and observed [$I > 2\sigma(I)$] reflections	364, 82, 81	286, 68, 67	362, 82, 74	343, 78, 70
R_{int}	0.019	0.020	0.023	0.021
$(\sin\theta/\lambda)_{max}$ (Å^{-1})	1.008	0.909	0.993	0.989
Refinement				
$R[F^2 > 2\sigma(F^2)]$, $wR(F^2)$, S	0.012, 0.046, 1.14	0.011, 0.038, 0.85	0.015, 0.054, 1.02	0.011, 0.045, 0.98
No. of reflections	82	68	82	78
No. of parameters	6	7	7	7
u	0.03324	0.03616	0.03942	0.03224
$\Delta\rho_{max}$, $\Delta\rho_{min}$ (fm Å^{-3})	0.35, −0.25	0.13, −0.12	0.12, −0.20	0.08, −0.13
Extinction coefficient	6.6 (4)	5.0 (3)	5.3 (4)	4.6 (3)

Weighting scheme based on measured s.u.'s, $w = 1/[\sigma^2(I) + (uI)^2]$. Computer programs: *NOMAD* (ILL, 2016), *RAFD9* (Filhol, 1988), *RACER* (Lehmann & Larsen, 1974; Wilkinson *et al.*, 1988), *SUPERFLIP* (Palatinus & Chapuis, 2007), *JANA2006* (Petříček *et al.*, 2014), *VESTA* (Momma & Izumi, 2011).

even for a distorted normal perovskite. Aware of this, Ludekens & Welch (1952) assigned BaLiF$_3$ the correct structure when first reporting its successful synthesis.

A variety of structural bulk defects in BaLiF$_3$ have been computed and discussed, amongst them LiF pseudo-Schottky defects as the thermodynamically most stable (Jackson *et al.*, 1996). However, more recent studies indicate that cation antisite defects, according to equation (1) (Zahn *et al.*, 2011; Düvel *et al.*, 2018), and fluoride–oxide substitution (from water vapour or carbon dioxide), according to equation (2) (Jackson & Valerio, 2002; Qiao *et al.*, 2009), are the most common intrinsic and extrinsic defects, respectively:

$$Ba_{Ba}^{\times} + Li_{Li}^{\times} = Ba_{Li}^{\bullet} + Li_{Ba}', \qquad (1)$$

$$2F_F^{\times} + H_2O = O_F' + V_F^{\bullet} + 2HF. \qquad (2)$$
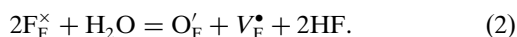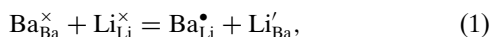
To our knowledge, the only neutron investigation on BaLiF$_3$ so far has been a study of inelastic scattering to record phonon dispersion curves (Boumriche *et al.*, 1994). Our own research interest in BaLiF$_3$ is due to the presence of two potentially mobile species, Li$^+$ and F$^-$, and their possible interplay. Based on high-temperature neutron diffraction, we will herein show that defects are indeed abundant in Czochralski-grown single crystals. Using topological and bond-valence methods, we will derive the preferred pathways for anion and (hypothetical) lithium-ion diffusion, as well as estimate the associated energy barriers.

2. Experimental

2.1. Sample preparation

A BaLiF$_3$ single crystal was grown using a Czochralski technique with automatic diameter control. The raw material,

a mixture of $x(BaF_2)$ = 43 mol% (single-crystalline chunks, Korth Kristalle GmbH) and $x(LiF)$ = 57 mol% (optical grade from GFI Advanced Technologies, Inc.), was premelted in a platinum boat under flowing HF gas according to the procedure described in more detail by Baldochi *et al.* (1996). The crystal was pulled from an inductively heated platinum crucible along the $\langle 111 \rangle$ direction at a rate of 2.0 mm h^{-1}. A variable crystal rotation between 10 and 25 min^{-1} was set to improve mixing of the melt and to avoid local occurrence of a constitutionally supercooled melt. The growth chamber was rinsed with a mixture of argon and CF$_4$ (φ = 10 vol.%) during the whole process. The crystal obtained was 18 mm in diameter and 75 mm long, and was colourless, transparent and free of macroscopic defects.

For neutron diffraction, a {100}-oriented cube of 5 mm × 5 mm × 5 mm was cut from a slice of the crystal. A shard-like fragment of the same slice with a suitable size was subjected to X-ray diffraction (for details, see §S1 in the supporting information).

2.2. Elemental analyses

The oxygen content was measured using a Leco EF-TC 300 N$_2$/O$_2$ analyser (hot-gas extraction). The absence of hydroxides was confirmed using a Thermo Finnigan FlashEA 1112 NC analyser. The content of barium, fluorine and lithium was quantified after alkali fusion with sodium and potassium carbonates (ζ = 1:1) in a platinum crucible. The barium content was measured gravimetrically following a standard protocol (Bracher *et al.*, 2003) and corrected against a reference specimen. The contents of fluorine and lithium were measured using a Dionex DX-120 ion chromatograph and a Thermo Fisher Scientific iCAP 6300 duo optical emission

spectroscope with an inductively coupled plasma, respectively. For the latter, the emission line at 610.3 nm was evaluated.

Anal. calcd for $BaLiF_{2.8}O_{0.1}$: Ba, 68.99; F, 26.72; H, 0.00; Li, 3.49; O, 0.80%. Found: Ba, 68.33; F, 26.73; H, 0.00; Li, 3.40; O, 0.14 (5)%.

2.3. High-temperature neutron diffraction

Diffraction data of a single crystal in vacuum glued to a titanium pin with high-temperature alumina-filled ceramic adhesive (Ceramabond 552) were collected at the hot-neutron four-circle diffractometer D9 at ILL (Grenoble, France) with Cu(220)-monochromated radiation (take-off angle $2\theta_M = 56.30°$) using ω and ω–2θ scans. Sample and beam stability were ensured by monitoring the (111) reflection in intervals of ~ 80 reflections. Data sets were acquired at 26.8 (3), 412 (3), 555 (3) and 636.2 (9)°C (Wiedemann, Fabelo et al., 2017). Data reduction was performed using *RACER* (Lehmann & Larsen, 1974; Wilkinson et al., 1988). An analytical absorption correction using Gaussian integration was employed with *JANA2006* (Petříček et al., 2014). Structures were solved with *SUPERFLIP* (Palatinus & Chapuis, 2007) using a charge-flipping algorithm.

2.4. Refinement details

Structures were refined with *JANA2006* against F_o^2 data using the full-matrix least-squares algorithm. A *SHELXL*-type extinction correction (Sheldrick, 2015) was applied. A weighting scheme based on standard uncertainties with a fixed instability factor (as derived from data merging) was employed. All ions were refined with fixed occupations in the final stage (see Table 1 for details).

Cationic displacement was modelled isotropically (constrained by site symmetry), whereas anharmonic displacement of the anions was modelled using the Gram–Charlier formalism. We attempted to refine parameters of the fourth and sixth order (those of the third and fifth order had to be zero for reasons of site symmetry) keeping only significant ones $[D_{ijkl} > 3\sigma(D_{ijkl})]$ in the refinement.

2.5. Maximum-entropy reconstruction

For the visualization of scattering length density (SLD) distributions, they were reconstructed from the final structure factors put out by *JANA2006* using maximum-entropy methods (MEM) as implemented in *Dysnomia* 0.9 (Momma et al., 2013). The unit cell was divided into $192 \times 192 \times 192$ voxels and set to contain the formula unit $BaLiF_{2.8}O_{0.1}$. Starting from a uniform intensity prior, the limited-memory Broyden–Fletcher–Goldfarb–Shanno (L-BFGS) algorithm (Nocedal, 1980) was employed with uncertainties augmented by $E = 0.5$ and relative weights λ_2, λ_4, and λ_6 for the generalized constraints chosen to give final central moments near unity ($\lambda_n = 0$ for orders $n > 6$; for details, see Table S2).

2.6. Topological analyses

Analysis of the procrystal void surface under exclusion of different ions was performed on ordered supercells using *CrystalExplorer3.1* (Wolff et al., 2012). For Voronoi–Dirichlet partitioning (VDP) analysis, *ToposPro5.3* (Blatov et al., 2014) was employed.

2.7. Bond-valence site energies (BVSE)

Bond-valence site energies (BVSE) were calculated using a beta version of the program *softBV* with a resolution of 0.1 Å based on published data (Adams & Rao, 2011). Substitutionally disordered crystals are best handled as statistically equivalent ordered supercells. Because of this, we computed the BVSE for lithium and fluoride ions using a randomly created $4 \times 4 \times 4$ supercell incorporating 180 F^- ($F_F^{\times}$), six O^{2-} (O_F') and six vacancies ($V_F^{\bullet}$) to mimic the composition determined *via* diffraction (see §S2). This resulted in the sum formula $LiBaF_{2.8125}O_{0.09375}$ (see Fig. S2).

3. Results and discussion

3.1. Structure and composition

Unlike with X-ray diffraction, the position of a lithium ion (scattering factor as high as $\sim -\frac{1}{3}$ of fluorine nucleus) can be clearly established using neutrons. In the present case, the models derived from structure solution (see Fig. 1) were identical to the established ones. However, we found that allowing occupancy reduction for the anion position improved the fit drastically (*e.g.* by $\Delta R_1 = 0.0114$, $\Delta wR_2 = 0.0441$ and $\Delta S = 1.08$ for all reflections at 26.8°C). At the same time, we observed neither a reduction of cation occupancies nor interstitial chunks of difference density that we could refine as additional fluoride positions. Furthermore, there is no indication of ample antisite defects, which would lead to a reduction of observed scattering length densities at both cation positions. We therefore concluded that oxide substitution (instead of Schottky or Frenkel defects) was the only appropriate model in our case. This view is corroborated by the results from barium, lithium and fluoride analyses (see §2.2): There is no significant deficiency in cations, which excludes ample Schottky defects, whereas the fluoride content is clearly lower than expected. Test refinements resulted in compliant fluoride/oxide occupancies (see §S2) so that we decided to fix the composition at $BaLiF_{2.8}O_{0.1}$. We attribute
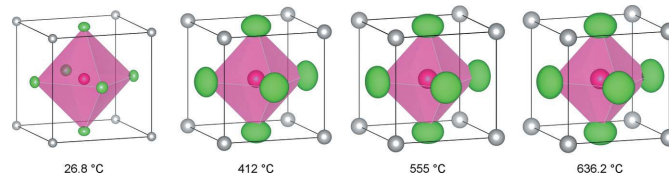

Figure 1
Crystal structures at different temperatures according to neutron diffraction (grey: barium, pink: lithium, green: fluoride/oxide ions; displacement ellipsoids at 90% probability, isosurfaces for probability density of 0.1 Å^{-3}; unit cell in black). *Caveat:* for 412°C and above, the anharmonically displaced anions are represented by a probability density isosurface that is not directly comparable to harmonic displacement ellipsoids.

the shortfall of the oxygen analysis to inaccuracies at very low contents.

Test refinements showed no significant anharmonic displacement of the lithium ion and only one significant anharmonic parameter (fourth order) for the anions at 412°C and above, which leads to an ever so slightly diamond-like shape of the probability-density isosurface (see green anions in Fig. 1). This observation is in accordance with the direction of optical phonon modes involving fluoride ions in perovskites (Nakagawa *et al.*, 1967) and with the statement that 'BaLiF$_3$ seems to be the least anharmonic [...] of the AMF$_3$ fluo[ro]perovskites' (Boumriche *et al.*, 1989). This means the small anharmonicity observed herein can be satisfactorily explained with lattice vibrations alone, *i.e.* not involving ion migration. This is further substantiated by the fact that, even at very low isovalues, the probability density surfaces describing the anionic displacement do not connect to continuous pathways.

An interesting peculiarity was observed in the plot of the unit-cell volume and the equivalent atomic displacement parameters against temperature (see Fig. 2). Although they grow in a monotonic fashion, the increase between 555 and 636.2°C is substantially larger/smaller than expected from linearity for the volume/displacement, respectively. The melting point of 826°C (Neuhaus *et al.*, 1967) is well above the experimental temperatures and cannot account for this irregularity. Thermodilatometric analysis on supposedly oxide-free single crystals grown in CF$_4$ atmosphere did not show such an anomaly (Bensalah *et al.*, 2003). A linear expansion coefficient of 3.33×10^{-5}°C^{-1} between 100 and 500°C was reported, whereas we estimate $2.83(6) \times 10^{-5}$°C^{-1} from neutron diffraction between 26.8 and 555°C (linear approximation).

3.2. MEM-reconstructed scattering-length density (SLD)

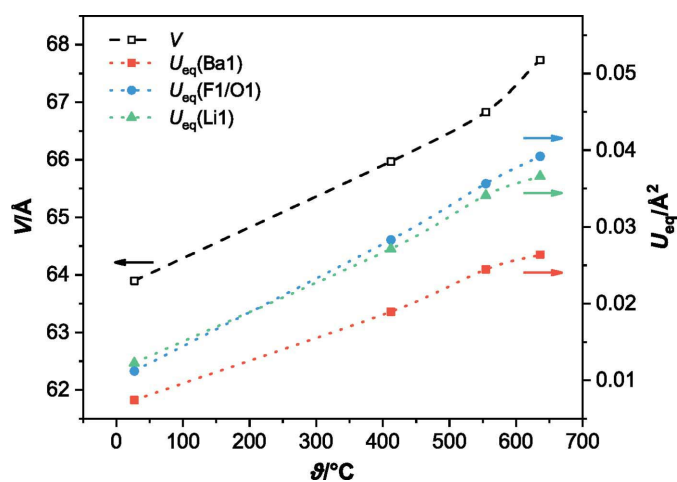To corroborate the anharmonic model of displacement, we had a closer look at the SLD (*i.e.* the neutron analogue of the electron density probed with X-ray diffraction) that we reconstructed using MEM. These methods yield the maximum variance of calculated structure factors within standard deviations of observed structure factors, in this way producing density maps, which contain less artefacts and are less prone to misinterpretation (Wiedemann *et al.*, 2016; Wiedemann, Islam *et al.*, 2017). These maps (see Fig. 3 for examples) show that the assessment is indeed correct: the pieces of SLD associated with the atomic positions do not connect to each other above noise level, thus indicating vibration instead of migration. The diamond-like anion distribution is also reproduced. In addition, we found small chunks of positive SLD at $(\frac{1}{2}, 0, 0)$ for isovalues lower than 3.95 (26.8°C) and 0.85 fm Å^{-3} (636.2°C). Their associated integral scattering lengths were, however, so small that a refinement as additional anion led to insignificant and/or negative occupation.

3.3. Procrystal-void analysis

As we were unable to map ion migration in BaLiF$_3$ single crystals experimentally, we have subjected the model derived from neutron diffraction at high temperature to state-of-the-art topological methods. In this way, we want to identify and assess the most probable pathways. One of the most easy-to-use method is the procrystal-void analysis, which maps the 'voidest' parts of the structure according to a procrystal model (spherically averaged, diffuse electron density).

The results show that the pathways accessible to anions run between adjacent positions roughly along the edges of the LiF$_6$ coordination octahedron [see Fig. 4(*a*)]. Around the equilibrium positions, empty space allows vibration in a diamond-like shape without strong distortion. Hypothetical lithium pathways between adjacent positions [see Fig. 4(*b*)] would run along $(\frac{1}{4}, \frac{1}{4}, \frac{1}{4})$ and $(\frac{1}{2}, 0, 0)$. However, the high isovalue of 0.0135 a.u., at which the pathways connect, indicates that they are in fact too narrow to conduct lithium ions. The only viable path for these ions would be a linear one through an anion vacancy [see Fig. 4(*c*)], leading to localized jumps instead of long-range transport.
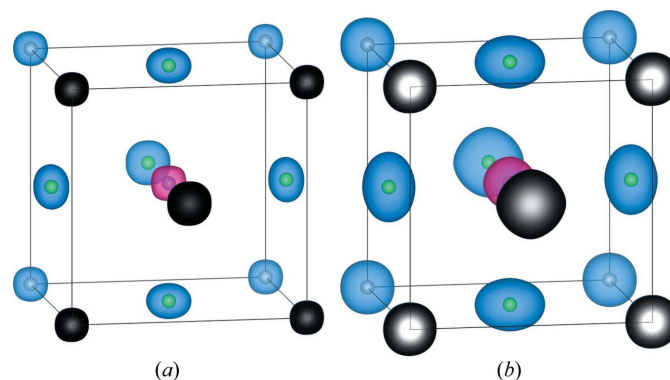

Figure 2
Unit-cell volumes V and equivalent displacement parameters U_{eq} for all ions at different temperatures (dotted and dashed lines merely guides to the eye, error bars smaller than symbols).

Figure 3
Isosurface representation of the SLD of ±1 fm Å^{-3} at (*a*) 26.8°C and (*b*) 636.2°C with (100) section through a Ba–F plane (blue: positive, pink: negative SLD; section in greyscale, white: maximum, black: near-zero SLD; ions with arbitrary radii; unit cell in black).

Table 2
Size and suitability of elementary voids and channels at room temperature and 636.2°C.

Elementary void	Position	Wyckoff position	R_{sd} (Å) (r.t., 636.2°C)	N† ($\Omega > 10\% \times 4\pi$)
Cation substructure				
ZA1	$\frac{1}{4}, \frac{1}{2}, 0$	12h	1.574, 1.605	0
Ba–F substructure				
ZA1	$\frac{1}{2}, 0, 0$	3d	1.240, 1.264	2
ZA2	$\frac{1}{4}, \frac{1}{4}, \frac{1}{4}$	8g	1.264, 1.288	1
ZA3	$\frac{1}{2}, \frac{1}{2}, \frac{1}{2}$ (Li1)	1b	1.240, 1.264	0

Elementary channel	R_{ch} (Å) (r.t., 636.2°C)
Cation substructure	
ZA1–ZA1	2.120, 2.162
Ba–F substructure	
ZA1–ZA2	1.632, 1.664
ZA2–ZA3	1.632, 1.664

† Number of interactions with ions with charge of the same sign. Criterion is the percentage of the full solid angle subtended by the respective ion.

3.4. Voronoi–Dirichlet partitioning (VDP)

VDP offers a deeper insight into the conduction pattern and allows geometrically rationalizing the viability of different pathways. For the tentative lithium conduction pattern, three types of elementary voids were detected [see Fig. 5(b) and Table 2], all of which *should be* slightly too small to accom-
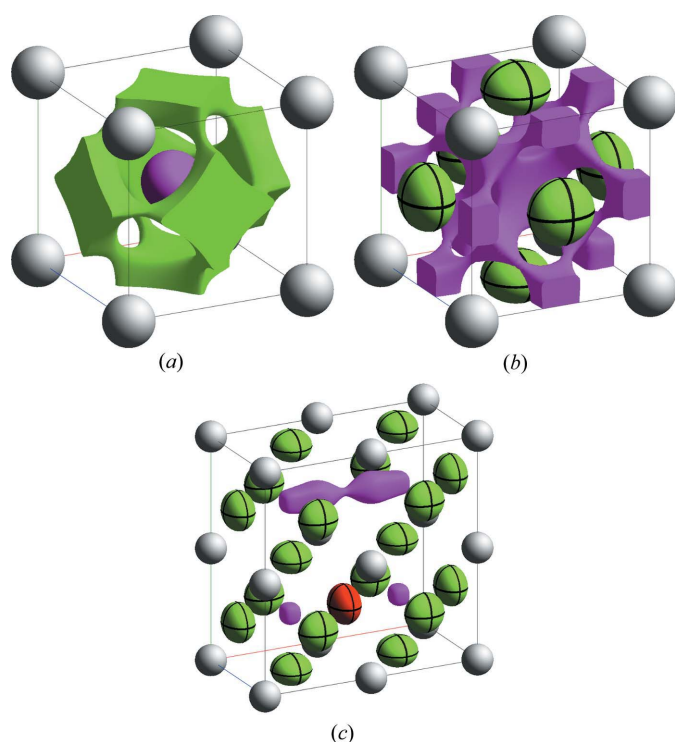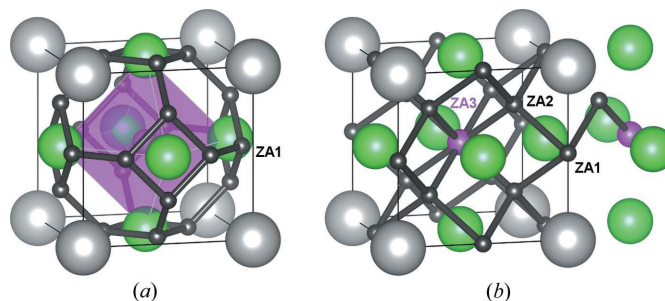

Figure 4
Procrystal-void surfaces at 636.2°C of (a) the [LiBa]$^{3+}$ framework at ρ_{pro} = 0.0081 a.u., the [BaF$_{3-2x}$O$_x$]$^-$ framework in (b) an averaged cell at ρ_{pro} = 0.0135 a.u. and (c) an ordered $2 \times 2 \times 1$ supercell at ρ_{pro} = 0.0049 a.u. (grey: barium, pink: lithium, green: fluoride, red: oxide ions; ellipsoids of 99% probability, harmonic contribution only).

Figure 5
Most probable pathways of (a) anion diffusion in the [LiBa]$^{3+}$ framework and of (b) lithium diffusion in the [BaF$_{3-2x}$O$_x$]$^-$ framework according to VDP analysis (grey: barium, pink: lithium, green: fluoride/oxide ions, black: major voids and channels; ions with ionic radii; unit cell in black).

modate lithium ions: they are characterized by spherical-domain radii $R_{sd} < 1.30$ (1) Å – a size which would be typical for lithium ions in fluoride environments (Blatov, 2004). As the centre of the smallest void type is in fact the crystallographic lithium position, it *can* actually host a lithium ion. Accordingly, we may not use this criterion strictly in our case. Nevertheless, all voids apart from the crystallographic lithium position exhibit at least one strong interaction with a barium ion (solid angle $\Omega >> 10\% \times 4\pi$) and are thus unfit to host a lithium ion. All elementary channels connecting the voids are too small for conduction: their radii R_{ch} are well outside of $R_{ch} \geq 1.76$ Å (90% of typical Li–F distance[2]). In summary, the elementary voids and channels are found to be probabilistic at best; the crystal is not a lithium-ion conductor. If, however, a lithium ion were to migrate, a path from one position Li1 to an adjacent one Li1′ *via* the VDP-determined void centres ZA2 and ZA1 would be the least disfavoured.

In contrast to this, only one type of elementary void is found in the anion conduction pattern. Interestingly, it does not coincide with the crystallographic anion position, but four voids are symmetrically arranged around the latter. They are fit to accommodate fluoride [R_{sd} = 1.59 (9) Å] or oxide ions [R_{sd} = 1.55 (12) Å] (Blatov & Serezhkin, 2000). The elementary channels are of two types: those connecting to other voids associated with the same anion position and those connecting to voids associated with an adjacent anion position. The former are determined by two interactions with lithium ions and one interaction with a barium ion, the latter *vice versa*. To assess the accessibility of the channels between neighbouring anions, using a weighted average of the anion–cation distances (F–Li: 1.76, O–Li: 1.85, F–Ba: 2.39, O–Ba: 2.48 Å; 90% of the typical distances[2]) is in order. The interaction-weighted distances of 2.18 and 2.27 Å for F$^-$ and O^{2-}, respectively, are only slightly greater than the channel radius. Thus, the crystal can be considered a moderately viable anion conductor.

---

[2] In the literature, these values are derived inconsistently. While mostly atomic radii according to Slater (1964) are employed [*e.g.* Li–O distance by Anurova *et al.* (2008)], they are sometimes calculated from ionic radii according to Shannon (1976) [*e.g.* Na–O distance by Blatov *et al.* (2006)]. We stuck to the former procedure for reasons of comparability.

3.5. Bond-valence energy landscape (BVEL)

In addition to the topology of preferred pathways, we were interested in an estimate of the associated migration barriers – a piece of information that bond-valence methodology offers. It describes the empirical mathematical relationship between bond strength and bond length (Brown, 2009). The bond valence s of a pair of atoms is most commonly represented by an exponential term with the statistically evaluated (and tabulated) bond-valence parameters R_0 and b and the measured interatomic distance R:

$$s = \exp[(R - R_0)/b]. \tag{3}$$

By summing up all bond valences of an atom and its neighbours, the bond-valence sum (BVS) of the respective atom is calculated. In an ideal case, the BVS is equal to its oxidation state. This concept works best with ionic materials but also reasonably well with covalent compounds.

Besides the verification of crystal structures and the prediction of positions of light elements such as lithium and hydrogen, the analysis and prediction of ionic conduction is one of the main applications of bond-valence methodology. For this purpose, the concept was successfully expanded to implement outer-coordination-sphere atoms (Adams, 2001) and introduce bond-valence sum mismatch (BVSM) between measured and ideal values (Adams, 2006). More recently, this BVSM was translated into bond-valence site energies (BVSE) using Morse-like potentials (Adams & Rao, 2011). The BVSE are calculated for every point in the unit cell. Their difference to the minimum, which is usually found at a crystallographic position of the ion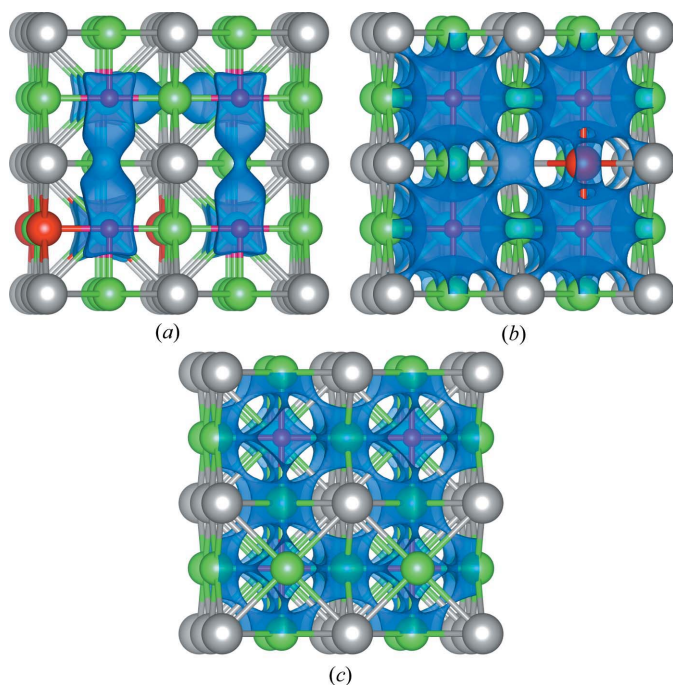 type under investigation, is an estimate of the energy necessary to displace it to that point (i.e. the migration energy). Together, the BVSE form the BVEL that shows the way of preferred migration as path of lowest energy difference between atomic sites.

To model anion vacancies and oxygen doping, we have performed calculations in a representative supercell (see Fig. S2) with the following results:

(a) The barrier for linear lithium migration through an anion vacancy is 2.08 eV [see Fig. 6(a), right side]. It is lowered to 2.07 eV if an oxide ion is coordinated to a neighbouring lithium ion or even 2.00 eV if an oxide ion is directly adjacent to the path [see Fig. 6(a), left side]. Accordingly, this could lead to local hopping at very high temperatures.

(b) With 3.04 eV, the barrier for lithium migration in the ideal structure via $(\frac{1}{4}, \frac{1}{4}, \frac{1}{4})$ and $(\frac{1}{2}, 0, 0)$ is too high to overcome in reality [see Fig. 6(b)].

(c) The barrier for fluoride migration via edges of LiF_6 octahedra is 0.64 eV [see Fig. 6(c)], enabling this process at medium temperatures.

However, these energies must be considered estimates as they account for neither defect formation nor relaxation near defects. These shortcomings can only be remedied using quantum-chemical computation.

4. Conclusion

Neutron diffraction indicated ample anion vacancies to be present in Czochralski-grown single crystals of the tentative composition $BaLiF_3$. We attribute this to oxide substitution, which is abundant in fluoride perovskite single crystals (Chadwick et al., 1983) and can as well happen after growth (Jackson & Valerio, 2002). While the anomaly in the temperature dependence of cell volume and atomic displacement parameters might be associated with processes like the dissociation or healing of defect pairs [e.g. $V_F^\bullet \cdot O_F'$ or $V_F^\bullet \cdot F_i'$ (Ziraps et al., 2001)], measurements with more temperature points have to be conducted first to rule out an artefact.

A model of the displacement of lithium ions and anions and a direct inspection of MEM-reconstructed SLD show anharmonicity for the anions at high temperature. However, this is adequately explained with lattice vibrations; ion migration, as would be indicated by connection of smeared SLD to continuous paths, was not observed. This means that thermally activated ion migration in the (in spite of the defects) highly ordered single-crystalline state is too sluggish to be mapped using this method, i.e. jumps are performed by too few individual ions during the experiment.

A variety of studies has shown that there is ionic conduction in powders as well as single crystals of $BaLiF_3$. Our analyses of the procrystal voids, the VDP, and the BVSE in the high-temperature structure[3] agree in the assessment that anions are potentially mobile in this structure, whereas lithium ions should be static. This corroborates the assumption that $BaLiF_3$

Figure 6
Details of the BVEL for the lithium ions at potential energies of (a) 2.1 and (b) 3.2 eV as well as (c) for the fluoride ions at a potential energy of 0.7 eV (grey: barium, pink: lithium, green: fluoride, red: oxide ions, blue: BVSE isosurface; ions with ionic radii).

---

[3] It should be noted that these methods are invariant to the amount of anion vacancies and substitution as they only depend on atomic positions and crystallographic symmetry.

electronic reprint

is an anion conductor (Kamata *et al.*, 1998; Rush *et al.*, 2001) and precludes lithium ions from playing a role in long-range transport. Any mobility of these (Düvel *et al.*, 2010, 2018) would be confined to anion vacancies, antisite defects or surfaces (Kunkel *et al.*, 2014). As these findings are founded on purely geometrical considerations (including ionic radii), they are valid not only for $BaLiF_3$ but also for all perovskites with similar ratios of ionic radii, *i.e.* for those with a near-ideal Goldschmidt tolerance factor $t \simeq 1$.

All three methods account for the diamond-like shape of anharmonic anion displacement asserted using neutron diffraction. This means that the directions of vibration correlate with the 'least occupied' parts of the crystal. Furthermore, the same pathway for anion migration is predicted: nearly linear and roughly along the edge of the LiF_6 octahedron. Inspection of the BVSE gives an estimate of 0.64 eV as the associated migration barrier. This is within reasonable range from the activation energy of $\sim$0.5 eV attributed to intrinsic conduction in $BaLiF_3$ single-crystals (Rush *et al.*, 2001; Düvel *et al.*, 2010). The difference indicates, on one hand, that defect formation plays indeed no role in the measured activation energies (else, they would have to be considerably greater) and, on the other hand, that local relaxation account for the lower barrier compared to the static BVSE model.

These considerations make it evident that the formation, existence, and healing of defects (especially anion vacancies) have a major influence on ion migration in the tightly packed perovskites. For this reason, neutron diffraction experiments on powders are ongoing.

Acknowledgements

References

Adams, S. (2006). *Solid State Ionics*, **177**, 1625–1630.
Adams, S. & Rao, R. P. (2011). *Phys. Status Solidi A*, **208**, 1746–1753.
Adams, S. (2001). *Acta Cryst.* B**57**, 278–287.
Anurova, N. A., Blatov, V. A., Ilyushin, G. D., Blatova, O. A., Ivanovschitz, A. & Dem'yanets, L. (2008). *Solid State Ionics*, **179**, 2248–2254.
Baldochi, S. L., Santo, A. M. E., Martins, E., Duarte, M., Vieira, M. M. F., Vieira, N. D. Jr & Morato, S. P. (1996). *J. Cryst. Growth*, **166**, 375–379.
Bensalah, A., Shimamura, K., Fujita, T., Sato, H., Nikl, M. & Fukuda, T. (2003). *J. Alloys Compd.* **348**, 258–262.
Blatov, V. A. (2004). *Crystallogr. Rev.* **10**, 249–318.
Blatov, V. A., Ilyushin, G. D., Blatova, O. A., Anurova, N. A., Ivanov-Schits, A. K. & Dem'yanets, L. N. (2006). *Acta Cryst.* B**62**, 1010–1018.
Blatov, V. A. & Serezhkin, V. N. (2000). *Russ. J. Inorg. Chem.* **45**, S105–S222.
Blatov, V. A., Shevchenko, A. P. & Proserpio, D. M. (2014). *Cryst. Growth Des.* **14**, 3576–3586.
Boumriche, A., Gesland, J. Y., Bulou, A., Rousseau, M., Fourquet, J. L. & Hennion, B. (1994). *Solid State Commun.* **91**, 125–128.
Boumriche, A., Simon, P., Rousseau, M., Gesland, J. Y. & Gervais, F. (1989). *J. Phys. Condens. Matter*, **1**, 5613–5620.
Bracher, F., Dombeck, F., Ettmayr, C. & Krauss, H.-J. (2003). *Arbeitsbuch quantitative anorganische Analyse*. Eschborn, Germany: Govi-Verlag.
Brown, I. D. (2009). *Chem. Rev.* **109**, 6858–6919.
Chadwick, A. V., Strange, J. H., Ranieri, G. A. & Terenzi, M. (1983). *Solid State Ionics*, **9–10**, 555–558.
Düvel, A., Morgan, L. M., Chandran, C. V., Heitjans, P. & Sayle, D. C. (2018). *Cryst. Growth Des.* **18**, 2093–2099.
Düvel, A., Wilkening, M., Uecker, R., Wegner, S., Šepelák, V. & Heitjans, P. (2010). *Phys. Chem. Chem. Phys.* **12**, 11251–11262.
Filhol, A. (1988). *RAFD9*. Institut Laue-Langevin, Grenoble, France.
Goldschmidt, V. M. (1926). *Naturwissenschaften*, **14**, 477–485.
ILL (2016). *NOMAD*. Institut Laue-Langevin, Grenoble, France.
Jackson, R. A. & Valerio, M. E. G. (2002). *Nucl. Instrum. Methods Phys. Res. B*, **191**, 32–36.
Jackson, R. A., Valerio, M. E. G. & de Lima, J. F. (1996). *J. Phys. Condens. Matter*, **8**, 10931–10937.
Kamata, M., Matsumoto, A. & Esaka, T. (1998). *Denki Kagaku Oyobi Kogyo Butsuri Kagaku*, **66**, 443–445.
Kunkel, N., Meijerink, A. & Kohlmann, H. (2014). *Phys. Chem. Chem. Phys.* **16**, 4807–4813.
Kurosawa, S., Yamaji, A., Pejchal, J., Yokota, Y., Ohashi, Y., Kamada, K. & Yoshikawa, A. (2017). *J. Mater. Sci.* **52**, 5531–5536.
Lehmann, M. S. & Larsen, F. K. (1974). *Acta Cryst.* A**30**, 580–584.
Ludekens, W. L. W. & Welch, A. J. E. (1952). *Acta Cryst.* **5**, 841.
Momma, K., Ikeda, T., Belik, A. A. & Izumi, F. (2013). *Powder Diffr.* **28**, 184–193.
Momma, K. & Izumi, F. (2011). *J. Appl. Cryst.* **44**, 1272–1276.
Nakagawa, I., Tsuchida, A. & Shimanouchi, T. (1967). *J. Chem. Phys.* **47**, 982–989.
Neuhaus, A., Holz, H. G. & Klein, H. D. (1967). *J. Phys. Chem.* **53**, 163–194.
Nocedal, J. (1980). *Math. C*, **35**, 773–782.
Palatinus, L. & Chapuis, G. (2007). *J. Appl. Cryst.* **40**, 786–790.
Petříček, V., Dušek, M. & Palatinus, L. (2014). *Z. Kristallogr. Cryst. Mater.* **229**, 345–352.
Qiang, Q., Guo, L., Han, L. & Wang, Y. (2016). *J. Nanosci. Nanotechnol.* **16**, 3715–3719.
Qiao, H., Liu, T., Zhang, Q., Cheng, F. & Zhou, X. (2009). *Nucl. Instrum. Methods Phys. Res. B*, **267**, 2467–2470.
Roy, R. (1954). *J. Am. Ceram. Soc.* **37**, 581–588.
Rush, G. E., Chadwick, A. V., Jackson, R. A., Valerio, M. E. G. & de Lima, J. F. (2001). *Radiat. Eff. Defects Solids*, **155**, 393–396.
Shannon, R. D. (1976). *Acta Cryst.* A**32**, 751–767.
Sheldrick, G. M. (2015). *Acta Cryst.* C**71**, 3–8.
Slater, J. C. (1964). *J. Chem. Phys.* **41**, 3199–3204.
Wang, W. W. (2014). The ESAB Group, Inc. WO2014164112A1.
Wiedemann, D., Fabelo, O. & Lerch, M. (2017). *Pathways of Cation and Anion Diffusion in BaLiF₃ Single Crystals*, Institut Laue-Langevin (ILL), Grenoble, France. doi: 10.5291/ill-data.5-14-261.

Wiedemann, D., Indris, S., Meven, M., Pedersen, B., Boysen, H., Uecker, R., Heitjans, P. & Lerch, M. (2016). *Z. Kristallogr. Cryst. Mater.* **231**, 189–193.

Wiedemann, D., Islam, M. M., Bredow, T. & Lerch, M. (2017). *Z. Phys. Chem.* **231**, 1279–1302.

Wilkinson, C., Khamis, H. W., Stansfield, R. F. D. & McIntyre, G. J. (1988). *J. Appl. Cryst.* **21**, 471–478.

Wolff, S. K., Grimwood, D. J., McKinnon, J. J., Turner, M. J., Jayatilaka, D. & Spackman, M. A. (2012). *CrystalExplorer3.1*. University of Western Australia, Perth, Australia.

Zahn, D., Herrmann, S. & Heitjans, P. (2011). *Phys. Chem. Chem. Phys.* **13**, 21492–21495.

Ziraps, V., Kulis, P., Tale, I. & Veispals, A. (2001). *Radiat. Meas.* **33**, 633–636.